# The influence of point defects on the entropy profiles of Lithium Ion Battery cathodes: a lattice-gas Monte Carlo study

Michael P. Mercer[1,*], Sophie Finnigan[1,4] Denis Kramer[2], Daniel Richards[3] and Harry E. Hoster[1]

[1]Department of Chemistry, Lancaster University, Bailrigg, Lancaster, LA1 4YB, United Kingdom

[2]Engineering Sciences, University of Southampton, Highfield, Southampton, SO17 1BJ, United Kingdom

[3]Imagination Lancaster, Lancaster University, Bailrigg, Lancaster, LA1 4YW, United Kingdom

*Corresponding author e-mail: m.mercer1@lancaster.ac.uk

In-situ diagnostic tools have become established to as a means to understanding the aging processes that occur during charge/discharge cycles in Li-ion batteries (LIBs). One electrochemical thermodynamic technique that can be applied to this problem is known as entropy profiling. Entropy profiles are obtained by monitoring the variation in the open circuit potential as a function of temperature. The peaks in these profiles are related to phase transitions, such as order/disorder transitions, in the lattice. In battery aging studies of cathode materials, the peaks become suppressed but the mechanism by which this occurs is currently poorly understood. One suggested mechanism is the formation of point defects. Intentional modifications of LIB electrodes may also lead to the introduction of point defects. To gain quantitative understanding of the entropy profile changes that could be caused by point defects, we have performed Monte Carlo simulations on lattices of variable defect content. As a model cathode, we have chosen manganese spinel, which has a well-described order-disorder transition when it is half filled with Li. We assume, in the case of trivalent defect substitution (M=Cr,Co) that each defect M permanently pins one Li atom. This assumption is supported by Density Functional Theory (DFT) calculations. Assuming that the distribution of the pinned Li sites is completely random, we observe the same trend in the change in partial molar entropy with defect content as observed in experiment: the peak amplitudes become increasing suppressed as the defect fraction is increased. We also examine changes in the configurational entropy itself, rather than the entropy change, as a function of the defect fraction and analyse these results with respect to the ones expected for an ideal solid solution. We discuss the implications of the quantitative differences between some of the results obtained from the model and the experimentally observed ones.

Keywords: Monte Carlo;  ;  ;  ;  , manganese spinel, entropy profiling, order/disorder transitions, point defects, solid solution

## 1. Introduction

The growing demand of rechargeable batteries for electric vehicles and stationary storage not only pushes for higher energy and power density but also improved durability and safety [1–

---

[4] Present address: Centre for Doctoral Training on the Theory and Simulation of Materials, Imperial College London, Exhibition Road, London, SW7 2AZ, United Kingdom

4]. Structural changes at the cathode during cell operation are one possible source of performance fade or failure. There has thus been an interest in developing in-situ methods to diagnose changes in the structure of the electrodes while the battery is in operation [5–9]. These methods can be contrasted with destructive post-mortem analysis techniques that yield very limited information concerning the cause of failure, under just one set of conditions [9–11]. To develop better understanding of cell aging a more quantitative understanding of existing in-situ characterisation tools is needed.

There has been an interest in techniques based on thermodynamic measurements. One method that has been developed is generally known as entropy profiling [8,9,12–28]. This technique is based on the principle that the partial molar entropy change is proportional to the temperature response of the open circuit potential (OCP) of a cell, by

$$\left(\frac{\partial E_{OCP}(x)}{\partial T}\right)_{p,x} = -\frac{1}{nF}\left(\frac{\partial S(x)}{\partial x}\right)_{p,T}, \qquad (1)$$

where $E_{OCP}$ is the open circuit potential, $T$ is the absolute temperature, $p$ is the pressure, $x$ is the amount of Li intercalated in the electrode ($0 < x < 1$), $n$ is the number of electrons transferred per atom, $F$ is the Faraday constant and the $S$ is the entropy [29]. Such profiles have been shown to reveal structural and thermodynamic information related to phase transitions to which other electrochemical techniques, such as slow rate cyclic voltammetry (SRCV) [6] and the incremental capacity method (ICM, also known as d$Q$/d$V$) [30] are not so sensitive.

The first entropy profile study was performed on $Li_xTiS_2$ electrodes by Thompson [12]. Selman *et al.* performed electrochemical-calorimetric measurements on $Li_xMn_2O_4$ [31] and commercial Li-ion cells [27]. Reynier *et al.* investigated the entropy change upon intercalation

into graphite and disordered carbons [17,22]. The entropy change during Li intercalation in graphite was also investigated theoretically by Leiva *et al.* [32][33].   Later work also investigated the entropy change in cathode materials, including $Li_xCoO_2$ [8,9,15,20], undoped $Li_xMn_2O_4$ spinel [13], $Li_{x+\delta}Mn_{2-\delta}O_4$ [14], where $\delta$ represents an excess amount of Li substituted in the octahedral sites [34,35], $Li_xM_yMn_{2-y}O_4$ [13,19,21,25], where M denotes a metal defect, and nickel manganese cobalt (NMC) based layered materials [24,36]. The cited studies have found that the features in these profiles arise from changes in the configurational entropy at the cathode upon (de-)intercalation, and hence the peaks and troughs observed correspond to structural, order/disorder, and other types of phase  transitions [8,18,19,37,38]. In the case of $Li_xCoO_2$, a vibrational component to the entropy changes has also been quantified [8]; however, this contribution is not strongly dependent of $x$ and has the effect of vertically shifting the profiles without affecting the peak amplitudes themselves. Furthermore, Maher *et al.* [9,23], Osswald *et al.* [24] and Hudak *et al.* [20] have examined the effect of prolonged charge/discharge cycles on the measured entropy profiles. They observed changes in the magnitudes of the peaks in profiles that were attributed to separate structural changes at the anode and cathode.

To better understand such profiles and enable more definitive structural assessments from them, a more quantitative understanding of the relationship between the peak amplitudes and the structure is needed. In the case of $Li_xMn_2O_4$ spinel, which is the focus of the present work, previous in-situ nuclear magnetic resonance (NMR) and X-ray diffraction (XRD) have revealed some contradictory results regarding phase transitions in the Li structure [14,39–41]; electrochemical thermodynamic measurements have revealed additional information about the phase diagram at room temperature and have added more insight into the two phase coexistence region [14,18,21]. The two peaks observed in the entropy profiles of this

electrode are generally considered to arise from the formation of an ordered phase, $Li_{0.5}Mn_2O_4$ at intermediate state of charge, and a transition to a disordered phase at high and low intercalation in the range $0 < x < 1$ [18,42–44]. A representative example of an entropy profile for this electrode overlaid with a result for $Li_xCr_{0.3}Mn_{1.7}O_4$ is shown in Figure 1. Manganese spinel with substitutional defects is one of the structurally simplest systems that is still of some commercial relevance.

In the present work, we examined the entropy profiles in manganese spinel cathodes which contain substitutional defects, M (where M = Cr, Co), i.e. $Li_xM_yMn_{2-y}O_4$, by Monte Carlo (MC) methods to gain a more quantitative understanding of the effect of point defect substitution on the entropy profile peak amplitudes. It is in line with previous works by us that used lattice gas MC to quantitatively relate experimental observation to theoretically predicted interaction energies [45–50]. The present work here uses the pairwise interaction model published elsewhere by Kim and Pyun [18] for $Li_xMn_2O_4$. We replicated some of the results from this work to check the energy expression and methodology. We extended the model to examine the effect of trivalent defect substitution, such as from $Cr^{3+}$ and $Co^{3+}$, on entropy profiles. Intentional substitution is commonly performed to improve the stability with respect to unmodified $Li_xMn_2O_4$. However, although there is an improvement in stability with metal substitution there is also a concomitant reduction in volumetric capacity [51,52]. Moreover, the changes observed in the entropy profiles during battery aging studies, namely a suppression of the peak amplitudes after successive charge/discharge cycles, could arise from the unintentional formation of point defects. We show changes in the entropy profiles related to the structure and quantitatively illustrate how these changes are related to the placement of irreversibly pinned Li sites. For the first time we also show the how the system configurational entropy itself varies along with the entropy changes that have previously been

reported. We then discuss the implications of these observations for experimental measurements.

*2. Calculations: Monte Carlo methods*

Figure 2 illustrates the well-known spinel lattice structure of $Li_xMn_2O_4$ (space group *Fd3m*) [3,53]. The Li sites, represented in gold, adopt a diamond lattice structure. In the region $0 < x < 1$, the Li sits in tetrahedral 8a sites, whereas Mn, which resides in the 16d positions, is coordinated to oxygen in the form of octahedra, as shown in Figure 2c. The oxidation state of the Mn ions can switch between +3 and +4 through a charge hopping mechanism [41,54]. Oxygen, which sits in the 32e sites, adopts a cubic close packed structure [3,53], The Li lattice can be thought of as two interpenetrating fcc sublattices, each of which is separated by a distance of (0.25,0.25,0.25). This formalism, which is represented in Figure 3a, is similar to that adopted elsewhere [18,42]. It is known that the structure can undergo irreversible distortions below room temperature and in the voltage region for which the amount of intercalated Li, *x*, is greater than 1. Here, we have only performed simulations at room temperature and within a voltage range 3.88 V < *E* < 4.30 V, where *E* is the applied voltage with respect to a Li anode. Under these conditions, the distortions are not applicable and *x* is constrained within the region $0 < x < 1$.

Within the model, nearest and second nearest neighbour pairwise interactions between Li atoms are considered. The nearest and second nearest neighbours are shown in Figure 3b.

Similarly to Kim and Pyun [18] we take as the Hamiltonian

$$H = J_1 \sum_i^N \left( \sum_j^{N_n} c_i c_j \right) + J_2 \sum_i^N \left( \sum_k^{N_s} c_i c_k \right) - (\varepsilon + \mu) \sum_i^N c_i, \tag{2}$$

where the interaction energy parameters relate to: $J_1$: nearest neighbour interaction $J_2$: second nearest neighbour interaction, $\varepsilon$: interaction between each Li atom and the $Li_xMn_2O_4$ spinel lattice. The other variables are: $\mu$: chemical potential; $c_i$: occupation number of site $i$; $c_j$ and $c_k$; occupation numbers of first and second nearest neighbours, respectively. $N_n = 4$ and $N_s = 12$: total number of possible nearest and second nearest neighbours (cf. Figure 3b), $N$: total number of lattice sites. The terms $c_i$, $c_j$ and $c_k$ take the value 1 if the site is occupied by Li; otherwise they are 0. The values of $J_1 = 37.5$ meV, $J_2 = -4.0$ meV and $\varepsilon = 4.12$ eV were determined by Kim and Pyun experimentally using gravimetric titration [18]; these values were used in all subsequent simulations including the structures with defect substitution. The main effect of substituting defects would be to modify the interaction parameter, $\varepsilon$, for Li atoms in the local vicinity of the substituted M sites. However, in the MC computations we treated these Li atoms as permanently pinned to the lattice, i.e. the same interaction parameter $\varepsilon$ was used for these atoms but any moves involving these atoms were not counted in the Monte Carlo algorithm. Further justification, based on DFT calculations, is provided in the Supporting Information, section 1. This calculation is based on the fact that the shift in the deintercalation potential of Li in the near neighbourhood of Co or Cr as determined by DFT (2.60 V and 1.52 V, respectively) is so large that the Boltzmann probability for deintercalation is negligible in both cases. In any case, we were interested in determining fluctuations in the internal energy, not the total energy value, of the lattice. $J_1$ and $J_2$ are Li-Li interaction terms and would not be affected significantly by the presence of M sites. Therefore, the pinned Li atoms contribute to the nearest and next nearest neighbour terms of the unpinned Li atoms in equation 2 with the same $J_1$ and $J_2$ values as previously stated.

The chemical potential, $\mu$, can be related to the equilibrium potential $E(x)$ with respect to a Li/Li$^+$ couple by $E(x) = - (\mu_{cathode}(x) - \mu_{anode})/e$, where $e$ is the electronic charge and $\mu$ is

expressed in eV. Taking the anode potential, $\mu_{anode}$, to be the standard chemical potential of metallic lithium, all potentials can be referenced with respect to the anode. Then $E(x) = E_{OCP}(x)$ = $-\mu_{cathode}(x)/e$, where $E_{OCP}(x)$ represents the experimentally observable open circuit potential of a Li-ion cell. This is consistent with the approach adopted by Ceder *et al.* [37] and Karlberg *et al.* [56]. However, in our simulations, $\mu = \mu_{cathode}$ is an input parameter that determines $x$ at any given electrode potential. Therefore

$$E = -\frac{\mu}{e}, \qquad (3)$$

and from now on, we refer only to the potential $E$ (vs. Li/Li$^+$) and chemical potential $\mu$.

To assess the effect of defect substitution on the lattice in $Li_xM_yMn_{2-y}O_4$, we started from the following assumptions:

1.  The placement of the defects, $M^{3+}$, into the lattice occurs entirely at random on the 16d sites. This is supported by X-ray diffraction (XRD) measurements of samples with $Cr^{3+}$ and $Co^{3+}$ substitutional defects, which did not detect the presence of any additional phases [25].

2.  The entire structure must remain charge neutral over the entire voltage range, 3.88 V $< E <$ 4.30 V.

3.  The valency of Mn can switch between 4+ and 3+ to maintain charge neutrality, as is generally accepted [4].

4.  If all other species in the structure are in their standard oxidation states, this implies that in order to maintain charge neutrality, exactly one Li atom per defect, M, must remain permanently pinned to the lattice, as suggested by Gao *et al.* [42]. This population can be called $x_{pinned}$, such that $x_{pinned} = y$, and the overall Li population, $x$,

can then be written as $x = x_{pinned} + x_{mobile}$, where $x_{mobile}$ is the Li population that can still (de-)intercalate.

5. In the model, the pinned Li atoms are treated equivalently to the mobile atoms as far as the nearest and next nearest neighbour summations in equation 2 are concerned, apart from the fact that they themselves never leave the lattice nor move.

6. Since the nearest neighbour Li atoms to each defect, M, reside with equal probability in each of the two sublattices, as shown in Figure 5, we assume that the population of Li that is pinned, $x_{pinned} = y$, is distributed randomly throughout the lattice.

The assumptions are similar to the ones presented in the work of Gao *et al.* [42], who examined Li intercalation in $Li/Li_{1+x}Mn_{2-x}O_4$. In that system, the only difference is that, based on charge conservation considerations, $3x$ Li atoms would be pinned, rather than $x$ as would be the case for trivalent defects. Another difference is that their model was based on a Bragg-Williams approach within a mean-field approximation, rather than also considering Li-Li interactions at each individual site as presented here.

Monte Carlo calculations were performed in two stages, using a home-built package written in Python 2.7.12. The first stage was a standard Metropolis Monte Carlo (MMC) algorithm [57] within a grand canonical ensemble (GCE), with spin flipping dynamics based on an Ising model [58]. The volume, $V$, of the cell and the temperature, $T = 298$ K, were kept fixed throughout the simulations. Periodic boundary conditions were applied to minimise edge effects. The lattice was a grid of 10 x 10 x 10 diamond unit cells, with 8 Li atoms per unit cell. We define the variable $s$, which relates to the effective number of lattice points on each side of the simulation cell, so that the full lattice was of size $s^3 = 8000$ points. The results obtained for variable system sizes are presented in the Supporting Information, section 2.3. The

chemical potential was initialised at a value where the Li content is negligible. A trial change in configuration was selected; if the change in energy, $\Delta H$, was greater than or equal to zero, the change was accepted automatically, otherwise, it was accepted with probability $P = \exp(-\Delta H / k_B T)$, where $k_B$ is the Boltzmann constant. By monitoring the occupancies in the two sublattices (as defined in Figure 3a), it was determined that a minimum of $3 \times 10^7$ Monte Carlo steps (MCS) per lattice were required for the lattice to achieve equilibrium. Once the lattice had reached this state, the chemical potential was increased, using the solution from the previous $\mu$ as the input lattice for the next one to reduce the equilibration period. The lattice state was saved once the solution had been reached for a particular value of $\mu$. This was performed for about 80 $\mu$ values in the interval -4.30 < $\mu$ < -3.88.

Statistical fluctuations in the occupancy, $N$, and internal energy, $U$, of the lattice were monitored separately. Using the saved lattice states as input files, parallel simulations were run. In each run, the MMC algorithm was performed as before. However, $N$ and $U$ were monitored by performing a summation over the entire lattice with a set sampling frequency. It was determined that sampling every 200 MCS gave the maximum number of samples over a given period of time on our cluster. For each parallel run, $2.4 \times 10^6$ MCS were performed, providing 12000 samples per run. By combining statistics from multiple runs, mean values and standard deviations in the parameters of interest could be monitored. For our main parameter of interest, the partial molar entropy, defined as

$$\left(\frac{\partial S}{\partial x}\right)_{V,T} = \frac{1}{T}\left[\frac{\text{Cov}(U,N)}{\text{Var}(N)} - \mu\right] = \Delta S \qquad (4)$$

where

$$\text{Cov}(U,N) = \langle UN \rangle - \langle U \rangle \langle N \rangle \qquad (5)$$

and

$$\mathrm{Var}(N) = \langle N^2 \rangle - \langle N \rangle^2, \qquad (6)$$

as shown elsewhere [59], many more parallel runs were required to reduce the size of the error bars than those of *<U>* and *<N>* themselves. Typically, at least 80 runs, or 960000 samples were required to reduce the size of the errors bars so that they were no longer visible. The long initial equilibration period was motivated by the much shorter time scale of the fluctuations than of macroscopic changes in the mean values of *U* and *N* themselves. However, a minimum of 2.4 x $10^6$ MCS was necessary to obtain accurate values for the entropy; running fewer MCS than this value resulted in systematically reduced partial molar entropy values which could not be detected by monitoring the error bar sizes. For the same reason, the error bars in *<U>* and *<N>* obtained by this method were not by themselves adequate descriptors of whether lattice equilibrium had been reached; this was only possible by carefully examining changes in the occupancies of the two sublattices. We further checked that the lattices had reached an equilibrium state by calculating voltammograms, as explained in Supporting Information section 2.1. We performed further analysis on the interactions in the system dependent on the defect content, using the peak widths of the calculated voltammograms. This analysis is presented in the Supporting Information, section 2.2.The partial molar entropy is actually equivalent to the quantity Δ*S* often referred to in the literature, even though strictly speaking it is a derivative with respect to the amount of Li intercalated, *x*, as defined in equation 1. To avoid confusion we will refer to the quantity from now on as ∂*S*/∂*x*.

For comparison and to check the consistency of our results, we generated results for an ideal solid solution within our model. These results were obtained by setting the parameters $J_1$ and

$J_2$ to 0, otherwise leaving the method unchanged from the one described above. The results obtained for the configurational entropy, $S$, were found to be equivalent to the analytical equation for the entropy of mixing of an ideal solid solution [60],

$$S = -R(x \ln(x) + (1 - x) \ln(1 - x)), \qquad (7)$$

where $R$ is the molar gas constant and in this case $S$ has been normalised to the number of moles of Li.

*3. Monte Carlo calculations: Results and Discussion*

*3.1 Li intercalation in Li$_x$Mn$_2$O$_4$*

Using Monte Carlo methods we first compare the results obtained for Li$_x$Mn$_2$O$_4$ with those expected for an ideal solid solution. Figure 5 shows the results for the variation in electrode potential, the variation in the occupancies of the two sublattices, the change in partial molar entropy, $\partial S/\partial x$, as well as the configurational entropy, $S$, itself. $S$ was obtained by integration of the result for $\partial S/\partial x$, shown in Figure 5b, with respect to $x$. Compared to the result for a solid solution, which comprises a single peak, the configurational entropy result for Li$_x$Mn$_2$O$_4$ arises due to the formation of an ordered phase which begins to deviate from the solid solution curve in the region $0.25 < x < 0.75$, as shown in Figure 5d. The sublattice occupancies in this region, Figure 5f-h, also show this deviation. Either side of that region, the structure fills completely randomly, i.e. it follows the solid solution curve. The pictures in Figure 5e and Figure 5i, obtained at high and low Li occupation respectively, support this observation.

The entropy results are best interpreted within the well-known Boltzmann definition of entropy [59],

$$S = k_B \ln(\Omega) \qquad (8),$$

where $\Omega$ is the number of real microstates (in this case, Li/vacancy arrangements) available in the system for a given macrostate. The difference between the curves for the solid solution and for the case of Li intercalation in $Li_xMn_2O_4$ arises because of the configurations that become unavailable due to the presence of the ordered phase rather than random filling or emptying. In the absence of any thermal fluctuations, the entropy would be zero at $x = 0.5$ as only a single configuration would be available corresponding to a perfectly ordered phase. However, at finite temperature, the resulting two peaks are not completely decoupled, but overlap at $x = 0.5$. Due to the symmetry, approximately the same number of configurations is available to the system during the filling of each sublattice, hence both peaks have nearly equal amplitudes.

The significance of the entropy value at $x = 0.5$ can be seen by looking at the dashed lines in Figure 5d. The fact that this value is not zero is due to the thermal fluctuation of Li from the ordered phase into the second sublattice, leaving behind a vacancy in the first. The same entropy value is obtained at the values $x \approx 0.05$ and $x \approx 0.95$, where the curves for Li intercalation in $Li_xMn_2O_4$ and the one for the solid solution overlay. Thus, a binary mixture of about 2.5 % vacancies and 2.5 % Li sites located out of the ordered structure is obtained at this value of $x$, in good agreement with the populations of the sublattices shown in Figure 5c and Figure 5g. Although to our knowledge the configurational entropy itself, rather than $\partial S/\partial x$, has never been directly examined from experimental entropy profiling measurements of Li-ion cathodes, the value of the local minimum of the integrated entropy $S$ could in principle be used as a metric to characterise the ordered phase in electrodes such as $Li_xMn_2O_4$. Recently, Leiva $et$ $al.$ analysed the entropy upon intercalation of Li into graphite using statistical mechanical approaches [33]. They obtained a similar result, displaying two entropy maxima, to the one presented here for $Li_xMn_2O_4$, as shown in Figure 2 of ref. [33].

The results in Figure 5a-c are in general agreement with the ones presented in Figure 1 of ref. [18]. These results replicate the ones of Kim and Pyun [18]; the simulations were performed to validate our model and test the correctness of our approach. The change in sublattice occupancy can be attributed to an order/disorder transition, as has been previously described for $Li_xMn_2O_4$ [18,53]. At the two extremes of potential, corresponding to Figure 5e and Figure 5i, both sublattices fill randomly and with equal probability. Consequently, the gradient of the voltage curve, which is related to $\partial S/\partial x$, follows that of a solid solution. However, due to the repulsive nearest neighbour interaction, in the intermediate voltage regime one of the sublattices is preferentially occupied over the other, as shown in Figure 5f-h, i.e. the Li/vacancy structure is ordered. This transition to an ordered phase is associated with a change in the derivative in the voltage curve, as remarked elsewhere [5,42,61]. For $x > 0.75$, although the gradient of the voltage curve is the same for Li intercalation in $Li_xMn_2O_4$ as for the ideal solid solution, the neglect of lateral Li-Li interactions in the latter case, corresponding to zero enthalpy of mixing [60], means that the two curves are vertically displaced from one another. This effect can be neglected for small $x$, thus the two curves coincide as $x$ tends to 0.

The reason for the formation of (local) minima and maxima in the plot of $\partial S/\partial x$ for $Li_xMn_2O_4$, shown in Figure 5b, can be understood by examining the pictures in the region of the order/disorder transition, Figure 5f-h. The lattice picture Figure 5f, coinciding with point 2 on Figure 5b, i.e. the minimum in $\partial S/\partial x$, shows that the first sublattice is the most occupied, yet there is still a significant population of vacancies in the lattice. As $x$ increases from 0.4 to 0.5, the vacancy population in the first sublattice quickly drops and reduces the number of configurations available. The concomitant steep decline in configurational entropy is reflected in the value of the local minimum of $\partial S/\partial x$. Close to the point 3 (Figure 5g), at $\partial S/\partial x$ = 0, the low fraction of Li that resides in the minority sublattice due to thermal fluctuations is

matched by the number of vacancies in the majority sublattice, i.e. $x = 0.5$ here. At the maximum in $\partial S/\partial x$, Figure 5h, the rapid rise in entropy between $x = 0.5$ and $x = 0.6$ is primarily associated with rapid filling of the second sublattice as $x$ increases.

*3.2 Influence of point defects: Li intercalation in $Li_x M_y Mn_{2-y} O_4$*

Figure 6 shows many of the same results from the previous section but for variable defect content.  Firstly, the variation in cell potential with respect to $x$ is plotted in Figure 6a; the same relationship is shown but with respect only to the mobile Li, $x_{mobile}$, in Figure 6b. As the number of defects, $y$, increases, the change in the derivative of the voltage curves in the vicinity of the order/disorder transition becomes suppressed, as explained previously elsewhere [14,38,42,61]. We have also shown the same curves with respect to the mobile Li because, in practice, it can be difficult to experimentally determine the amount of pinned Li with a sufficient accuracy, which in turn can lead to experimental uncertainties in the determination of capacities (i.e., the quantitative correlation between Li content of the cathode and the relative SOC) [62]. For completeness, the results are also plotted with respect to the cell potential as is often reported experimentally [20,23].

<InlineImage6>
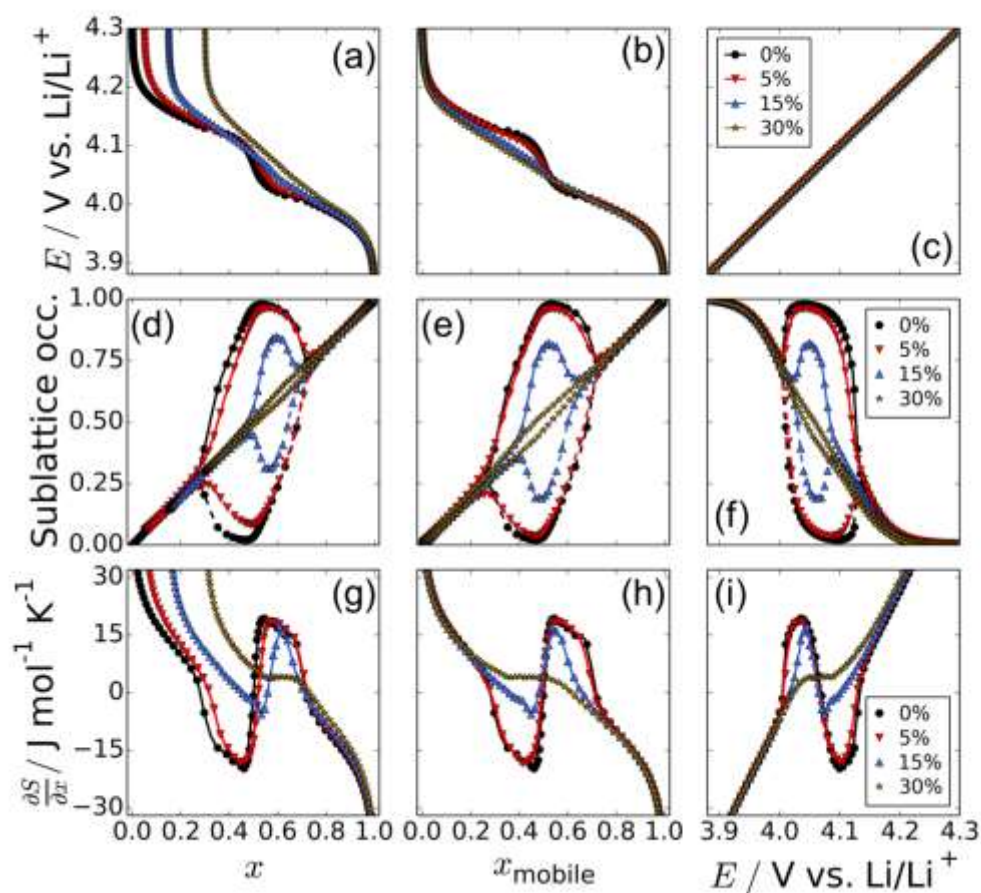
Figure 6. Effect of varying the defect content, and hence the amount of pinned Li, as a function of $x$, the total proportion of Li in the lattice (left column) and as a function of the total fraction of mobile Li, $x_{mobile}$ (middle column), and as a function of potential (right column). The variation in electrode potential (first row), sublattice occupancies (middle row) and partial molar entropy (bottom row) are all shown. Note, for clarity: in (e) and (f), the sublattice occupancies were normalised to the amount of mobile Li, in (d), they are normalised to the total amount of Li.

<InlineShape5>

The origin of the change in the voltage profiles can be seen most clearly in Figure 6d-f, which show the change in the occupancy of the sublattices with respect to $x$, $x_{mobile}$ and the electrode potential dependent on the defect concentration, $y$. Figure 6e, plotted as a function of the

mobile Li only, shows that only 5 % defect incorporation results in a slight change in the occupations of the two sublattices. This is also consistent with the entropy profiles, plotted in Figure 6g-i, which show a very slight reduction in peak amplitude but are otherwise very similar to the result for $y$ = 0 %. Due to the presence of 5 % Li permanently pinned to the lattice there is also a slight shift in the peak positions. The shift is dependent on the measurement of the Li content; the peaks are shifted with respect to the total Li content, $x$. However, there is no apparent shift in peak position with respect to the mobile Li content or the electrode potential. Thus the peak potentials are determined by the Li atoms that are available to (de-)intercalate and not the overall Li content.

As the defect content is progressively increased from $y$ = 15 % and then $y$ = 30 % a more marked decrease in peak magnitude is observed. Furthermore, the result obtained for $y$ = 15 % suggests that the magnitudes of the two peaks are not suppressed equally by the presence of the defects as might be naively expected; rather the local minimum at $x_{mobile} \approx 0.45$ has a smaller amplitude than the local maximum at $x_{mobile} \approx 0.55$. This observation also holds for $y$ = 5 %, although the effect is more subtle. The result for $y$ = 30 % indicates a voltage and partial molar entropy profile that closely resembles a solid solution; i.e. the peak and trough corresponding to the order/disorder transition are hardly visible at all. This is consistent with the images presented in Figure 6d-f, which show that the occupancies are split almost equally between the two sublattices over the entire intercalation range.

Further insight into these effects can be gained by comparing the entropy changes, $\partial S/\partial x$, with the entropy itself, $S$. These results are shown in Figure 7. In particular, by examining Figure 7b, the difference in the amplitudes of the two peaks for the same defect content $y$ becomes more obvious than looking only at the changes with respect to $\partial S/\partial x$. Asymmetries

in the peak magnitudes have been observed experimentally in $Li_xMn_2O_4$ [13], overlithiated $Li_{1+x}Mn_{2-x}O_4$ [14] and also $Li_xM_yMn_{2-y}O_4$ [21,25] although not previously remarked upon. The origin of the peak magnitude difference can be observed in Figure 8, which shows how the sublattice occupancies vary as a function of potential as well as Li content. The situation is very similar for all $y$ values at high potential $E$ = 4.15 V, as shown by comparing Figure 8a-d, and also at $E$ = 3.95 V, as shown in Figure 8i-l. This is consistent with the very similar results for $\partial S/\partial x$ and S obtained at the two extremes of potential regardless of the defect content, as shown in Figure 7, i.e. solid solution filling is observed at the potential extremes. At $E$ = 4.05 V, in the region where the ordered phase forms for $y$ = 0 %, the presence of the pinned Li sites disrupts the formation of the ordered phase and forces a greater fraction of Li onto the minority sublattice, as shown in Figure 8e-h. The result is that the length scale of the ordered phase decreases as y increases, until at $y$ = 30 % (Figure 8h), almost random filling is observed.

Further, the packing density of the structures formed at intermediate potentials 4.05 V < $E$ < 4.20 V is less efficient than the ordered phase shown in Figure 8e, which results in a higher vacancy population at a given potential. This point is further supported by Figure 6b, which shows that the overall occupation of mobile Li in the same potential region decreases with respect to the defect content. Also, in Figure 8f-h, a progressively higher vacancy population is observed as the defect content increases. These vacancies appear to reside with high probability in the near neighbourhood of pinned Li sites in the minority sublattice, as most clearly demonstrated in Figure 8f and 8g. The configurations that are unavailable when filling the lattice between 0 < $x_{mobile}$ < 0.5 are regained in the interval 0.5 < $x_{mobile}$ < 1, resulting in the observed difference in the amplitudes of the two peaks for all the crystal structures with $y$ > 0%. This is best shown by comparing the curve for $y$ = 30 % with the solid solution result in Figure 8b. The extra vacancies that are filled between 0.5 < $x_{mobile}$ < 1 result in a greater

number of configurations available, which distorts the shape of the curve from that obtained for an ideal solid solution. The entropy magnitude is also reduced with respect to the solid solution because of the restricted number of removable Li sites.

### 3.3 Analysis of entropy profile amplitudes

As an appropriate parameter to compare the simulated and experimental results, we examined the combined amplitude of the peak and trough in the entropy profiles, a parameter demonstrated in Figure 1. The advantage of this approach over comparing the individual peak amplitudes is that any possible error resulting from a downwards shift in the entropy profiles due to vibrational entropy contributions, as has been identified in $Li_xCoO_2$ [8], is eliminated. Physically, this amplitude represents the combined effect of fluctuations due to vacancies during filling of the ordered phase between $0.4 < x_{mobile} < 0.5$, followed by filling of less energetically preferred nearest neighbour sites between $0.5 < x_{mobile} < 0.6$. In Figure 9, we show the relationship amplitude of the entropy maximum, the entropy minimum and the combined amplitude of both entropy peaks (defined in Figure 1).

Figure 9 shows a non-linear decrease in the overall entropy amplitude as a function of the defect content. This can be understood by examining the amplitudes of the two individual peaks, whose sum gives the overall amplitude. Up to a defect percentage of about 14 %, the amplitudes of the entropy maximum do not vary significantly with defect content, except for some slight scatter due to random variations between simulations. However, a slow decrease in the amplitude of the minimum results in a gradual decrease in the overall amplitude. As the defect percentage increases to about 8-10%, the rate of decrease of the amplitude of the minimum becomes greater; between about 14-15 %, the maximum value also begins to decrease. We explain the faster rate of decrease in the amplitude of the minimum with

respect to that of the maximum due to the preferential formation of vacancies in the near neighbourhood of the pinned Li sites, as explained in section 3.1.2. The difference between the variation in the maximum and minimum amplitudes then explains the non-linear trend in the overall amplitude with the defect amount.

We considered the possibility that the entropy amplitude is related in some way to the short range order in the Li-vacancy structures. We can define the Warren-Cowley short range order (SRO) parameter

$$\gamma(r) = 1 - \frac{P_{AB}(r)}{x}, \qquad (9)$$

where $\gamma(r)$ is the SRO parameter within a coordination sphere of radius $r$, $P_{AB}$ is the probability that an AB pair resides at that radius, and $x$ is the atomic fraction of B [63]. Here, A = vacancy and B = Li atom. A value of $\gamma$ = 0 across the entire potential range indicates no preference for ordering in the Li distribution, i.e. an ideal solid solution. We considered SRO parameters for values of $r$ corresponding to nearest neighbour and second nearest neighbour pairs, which we denote $\gamma_1$ and $\gamma_2$, respectively. The variation in these parameters is shown in Figure 10.

(b)
<InlineShape3>

The plots in Figure 10 show that the Li/vacancy structure becomes progressively more ordered as $x_{mobile}$ tends towards 0.5. Either side, the structure becomes less ordered. Furthermore, the absolute magnitude of the peak decreases systematically as a function of the defect fraction, providing a quantitative indication of the suppression of the order/disorder transition. The reason that $\gamma_1$ and $\gamma_2$ are so close in magnitude but opposite

in sign, is that during the formation of the ordered phase, only one of the sublattices is occupied. Consequently, Li is preferentially located by first nearest neighbour vacancies, implying a negative value of $\gamma_1$. However, the second nearest neighbours reside in the same sublattice as the reference site. Thus, in the ordered phase, occupation of a site by Li implies with high probability that its second nearest neighbours are also occupied, and so $\gamma_2$ is positive.

Figure 11a shows the defect fraction plotted as a function of the maximum value of the first SRO parameter, $\gamma_1$, as shown in Figure 10a. The partial molar entropy peak amplitudes are shown with respect to $\gamma_1$ in Figure 11b. The results reveal an approximately linear relationship between $\gamma_1$ and the defect content, for $y \leq 17$ %. The relationship is no longer linear at $y = 30$ %, which reveals that the nature of the disruption to the order/disorder transition becomes more complex at higher defect contents. We don't have a complete explanation and will investigate this phenomenon further in future work. The non-linear relationship between the entropy peak amplitude and the defect content, as shown in Figure 9, is also reflected in the relationship between the same amplitude and $\gamma_1$ shown in Figure 11b. Thus the suppression of the peak amplitude with increasing defect content is related to short range order in the Li/vacancy structure, and possibly also the Li-M structure for higher defect amounts. However, since the individual peaks are not suppressed equally, further work is needed to provide a full explanation for the observed relationship.

(b)
<InlineShape1>

Lastly, we compare the simulated and experimental entropy peak amplitudes. These results are shown in Table 1. The simulated results can be considered to be applicable to either Co

or Cr substitution, since in both cases, the binding energy shift is so large that the Li atoms neighbouring the defect would be permanently pinned.

There are still only limited experimental studies that systematically examined the effect of defect concentration on entropy profiles. Most of the work compared the entropy changes at only one defect concentration with the ostensibly defect free $Li_xMn_2O_4$ [13,14,19,21], from which it is difficult to draw quantitative conclusions. The most complete study for trivalent defects (M = Cr, Co) was performed by Kashiwagi $et\ al.$ [25].  Qualitatively, their voltage profiles show a suppressed slope in the vicinity of $x$ = 0.5 as the defect content is increased, just as our model shows. Their experimental entropy profiles show a reduction in peak magnitude as a function of $y$, again in agreement with our simulations. The same trends were experimentally observed by Kobayashi $et\ al.$ with M = Cr and $y$ = 30 % [21], Gao $et\ al.$ in $Li_{1+x}Mn_{2-x}O_4$ (0 < $x$ < 1) [42] and Thomas $et\ al.$ in $Li_xMn_{1.8}Al_{0.2}O_{4-\delta}F_{0.2}$ [13].

The results suggest good agreement between the simulations and the experimental results for defect content, $y$ ≤ 15 %. There are, however, some important quantitative differences, notably between the results of Kobayashi $et\ al.$ [21] and Kashiwagi $et\ al.$ [25] at  $y$ = 30 %. In our simulations, the results for the entropy profiles obtained at $y$ = 30 % are very similar to the one for a solid solution, as shown in Figure 7a, except for the presence of a small shoulder. While the features attributable to the order/disorder transition are suppressed with respect to the results obtained for $y$ = 0 %, those features are still clearly visible in the experimental results, as shown for example in Figure 1 of ref. [21]. One possibility is that the experimental samples for $y$ = 30 % display partial or full phase segregation. This would mean that there would defect deficient regions where the transition could still occur. However, at least from the XRD results of Kashiwagi $et\ al.$, no long ranged phase segregation was observed [25].

Our simulations assume that the pinned Li distribution is entirely random. While this may be an adequate approximation for $y < 30\%$, in the case $y = 30\%$, repulsive interactions between the pinned Li would likely make clusters of them as mutual nearest neighbours, arising by chance simply due to the high population, highly energetically unfavourable. We did not include the effect of possible short range order in the substituted metal M distribution in the simulations; including these effects might then have implications for the short range order in the pinned Li distribution, and in turn, the partial molar entropy peak magnitude. Additionally, while our assumption that the pinned Li sites are constrained within the orbit of the defect M, as shown in Figure 4, can be justified [42], our present model does not allow the Li to move within those orbits. We intend to develop a future model that can account for motion of the Li in the vicinity of the defects.

*4. Conclusions*

We have examined the change in partial molar entropy as a function of the Li content in perfectly crystalline $Li_xMn_2O_4$. As has been previously found, we find that features observed in the profile are due to an order/disorder transition in the Li sublattice. This can be visualised by considering the Li sublattice itself as two separate fcc sublattices, only one of which is occupied in the ordered phase, except for a small fraction of the sites which move into the opposite sublattice due to thermal fluctuations.

We extended the model to investigate Li intercalation in $Li_xM_yMn_{2-y}O_4$ as a model system with point defects, where the defects can be Co or Cr (valency +3). With this method we also simulated the possible effect of unintentional point defect substitution arising from cell aging. From electrostatic arguments, and supported by DFT calculations, considered we assumed a random distribution of Li permanently pinned to the lattice, $x_{pinned}$, equivalent to the defect

concentration, $y$. On the basis of the results of this model the following conclusions can be drawn:

1. Consistently with the known experimental results, the presence of the defects suppresses the overall amplitude of the two entropy profile peaks. Through repulsive nearest neighbour interactions, the pinned Li sites reduce the energy gain that would result from ordering.

2. The amount by which the peaks are suppressed increases with the defect content $y$. A higher $y$ value forces the mobile Li to reside in smaller and smaller domains. In the most extreme case examined, defect percentage, $y = 30\,\%$, the entropy profile peaks are barely discernible and the result tends to one close to that of a solid solution over the entire voltage range.

3. Consistently with previous experiments and models, a change in gradient in the voltage profile as a function of the mobile Li content is observed for $Li_xMn_2O_4$ at $x = 0.5$. However, as the defect concentration increases, the change in gradient in the potential region of the order/disorder transition (between about 4.00 V and 4.15 V) becomes progressively less pronounced.

4. There are some quantitative discrepancies between the experimentally observed entropy profiles and the simulated ones. The model suggests a more pronounced suppression of the peaks associated with the order/disorder transition at high defect content ($y \approx 30\,\%$) than is observed experimentally. However, good quantitative agreement is obtained for $y \leq 15\,\%$. To resolve some of the quantitative differences between the model and the simulated results observed for high defect content in the entropy peak amplitudes, in future work we plan to include the effect of motion of the Li atoms confined within the radius of the defect atoms.

5. We considered the possibility that the partial molar entropy peak profile is related to the short range order in the Li/vacancy structure. The short range order analysis revealed an approximately linear relationship between the Warren-Cowley parameter and the defect content, for $y \leq 17\%$. Due to the complex dependence of the amplitude of the two individual peaks on the defect content, a non-linear trend of the overall amplitude on the defect content was determined. For the accurate quantification of entropy profile peaks at high defect content ($y \geq 30\%$), a future model would need to account for short range ordering in the substituted metal M distribution, which could then affect the pinned Li/vacancy distribution and in turn, the entropy profile peak amplitudes.

6. For the first time, we also examined the effect of the defect content on the absolute configurational entropy. These results provide additional insight into the origin of the difference in peak amplitude that has sometimes been observed in $Li_xMn_2O_4$ and spinel electrodes with intentional substitutional defects. Going from $x = 0$ to $x = 1$, the difference between the amplitude of the two peaks becomes more pronounced as the defect content increases. We attribute this effect to the presence of extra vacancies in the near neighbourhood of the pinned Li sites.

*References*

[1]     M.S. Whittingham, Lithium batteries and cathode materials, Chem. Rev. 104 (2004) 4271–4301. doi:10.1021/cr020731c.

[2]     J.B. Goodenough, Y. Kim, Challenges for rechargeable Li batteries, Chem. Mater. 22 (2010) 587–603. doi:10.1021/cm901452z.

[3]     M.M. Thackeray, Manganese oxides for lithium batteries, Prog. Solid State Chem. 25 (1997) 1–71. doi:10.1016/S0079-6786(97)81003-5.

[4]     M.M. Thackeray, Y. Shao-Horn, A.J. Kahaian, K.D. Kepler, E. Skinner, J.T. Vaughey, S. a Hackney, Structural Fatigue in Spinel Electrodes in High Voltage (4 V) Li/LixMn2O4 Cells, Electrochem. Solid-State Lett. 1 (1998) 7–9. doi:10.1149/1.1390617.

[5]     L. Zhou, M. Leskes, T. Liu, C.P. Grey, Probing dynamic processes in lithium-ion batteries by in situ NMR spectroscopy: Application to Li1.08Mn1.92O4 electrodes, Angew. Chemie - Int. Ed. 54 (2015) 14782–14786. doi:10.1002/anie.201507632.

[6]     Y. Merla, B. Wu, V. Yufit, N.P. Brandon, R.F. Martinez-Botas, G.J. Offer, Novel application of differential thermal voltammetry as an in-depth state-of-health diagnosis method for lithium-ion batteries, J. Power Sources. 307 (2016) 308–319. doi:10.1016/j.jpowsour.2015.12.122.

[7]     L.A. Godinez, J. Lin, M. Marc, Electrochemical and In Situ X-Ray Diffraction Studies of Lithium Intercalation in LixCo02, J. Electrochem. Soc. 139 (1996) 2091–2097.

[8]     Y. Reynier, J. Graetz, T. Swan-Wood, P. Rez, R. Yazami, B. Fultz, Entropy of Li
        intercalation in LixCoO2, Phys. Rev. B - Condens. Matter Mater. Phys. 70 (2004) 1–7.
        doi:10.1103/PhysRevB.70.174304.

[9]     K. Maher, R. Yazami, Effect of overcharge on entropy and enthalpy of lithium-ion
        batteries, Electrochim. Acta. 101 (2013) 71–78. doi:10.1016/j.electacta.2012.11.057.

[10]    T. Waldmann, M. Wilka, M. Kasper, M. Fleischhammer, M. Wohlfahrt-Mehrens,
        Temperature dependent ageing mechanisms in Lithium-ion batteries - A Post-Mortem
        study, J. Power Sources. 262 (2014) 129–135. doi:10.1016/j.jpowsour.2014.03.112.

[11]    D. Aurbach, B. Markovsky, A. Rodkin, M. Cojocaru, E. Levi, H.J. Kim, An analysis of
        rechargeable lithium-ion batteries after prolonged cycling, Electrochim. Acta. 47
        (2002) 1899–1911. doi:10.1016/S0013-4686(02)00013-0.

[12]    A.H. Thompson, Thermodynamics of Li intercalation batteries: Entropy measurements
        on LixTiS2, Phys. B+C. 105 (1981) 461–465. doi:10.1016/0378-4363(81)90295-3.

[13]    K.E. Thomas, C. Bogatu, J. Newman, Measurement of the Entropy of Reaction as a
        Function of State of Charge in Doped and Undoped Lithium Manganese Oxide, J.
        Electrochem. Soc. 148 (2001) A570. doi:10.1149/1.1369365.

[14]    R. Yazami, Y. Reynier, B. Fultz, Entropymetry of Lithium Intercalation in Spinel
        Manganese Oxide: Effect of Lithium Stoichiometry, ECS Trans. 1 (2006) 87–96.

[15]    K.E. Thomas, J. Newman, Heats of mixing and of entropy in porous insertion
        electrodes, J. Power Sources. 119–121 (2003) 844–849. doi:10.1016/S0378-
        7753(03)00283-0.

[16]    W. Lu, I. Belharouak, S.H. Park, Y.K. Sun, K. Amine, Isothermal calorimetry

investigation of Li1+xMn2-yAlzO4 spinel, Electrochim. Acta. 52 (2007) 5837–5842. doi:10.1016/j.electacta.2007.03.005.

[17]     Y.F. Reynier, R. Yazami, B. Fultz, Thermodynamics of Lithium Intercalation into Graphites and Disordered Carbons, J. Electrochem. Soc. 151 (2004) A422. doi:10.1149/1.1646152.

[18]     S. Kim, S. Pyun, Thermodynamic and kinetic approaches to lithium intercalation into a Li1−δMn2O4 electrode using Monte Carlo simulation, Electrochim. Acta. 46 (2001) 987–997.

[19]     H. Bang, H. Yang, Y.K. Sun, J. Prakash, In Situ Studies of Li x Mn2 O 4 and Li x Al0.17Mn1.83 O 3.97 S 0.03 Cathode by IMC, J. Electrochem. Soc. 152 (2005) A421–A428. doi:10.1149/1.1851035.

[20]     N.S. Hudak, L.E. Davis, G. Nagasubramanian, Cycling-Induced Changes in the Entropy Profiles of Lithium Cobalt Oxide Electrodes, J. Electrochem. Soc. 162 (2015) A315–A321. doi:10.1149/2.0071503jes.

[21]     Y. Kobayashi, Y. Mita, S. Seki, Y. Ohno, H. Miyashiro, M. Nakayama, M. Wakihara, Configurational Entropy of Lithium Manganese Oxide and Related Materials, LiCryMn 2−yO4 (y=0, 0.3), J. Electrochem. Soc. 155 (2008) A14. doi:10.1149/1.2799069.

[22]     Y. Reynier, R. Yazami, B. Fultz, The entropy and enthalpy of lithium intercalation into graphite, J. Power Sources. 119–121 (2003) 850–855. doi:10.1016/S0378-7753(03)00285-4.

[23]     K. Maher, R. Yazami, A study of lithium ion batteries cycle aging by thermodynamics techniques, J. Power Sources. 247 (2014) 527–533.

doi:10.1016/j.jpowsour.2013.08.053.

[24]    P.J. Osswald, M. Del Rosario, J. Garche, A. Jossen, H.E. Hoster, Fast and Accurate

Measurement of Entropy Profiles of Commercial Lithium-Ion Cells, Electrochim. Acta.

177 (2015) 270–276. doi:10.1016/j.electacta.2015.01.191.

[25]    T. Kashiwagi, M. Nakayama, K. Watanabe, M. Wakihara, Y. Kobayashi, H. Miyashiro,

Relationship between the electrochemical behavior and Li arrangement in LixMyMn2-

yO4 (M = Co, Cr) with spinel structure, J. Phys. Chem. B. 110 (2006) 4998–5004.

doi:10.1021/jp056334y.

[26]    N. Kumagai, T. Fujiwara, K. Tanno, Thermodynamic and Kinetic Studies of

Electrochemical Lithium Insertion into Quaternary Li-Mn-V-O Spinel as Positive

Materials for Rechargeable Lithium Batteries, J. Electrochem. Soc. 140 (1993) 3194–

3199. doi:10.1149/1.2221009.

[27]    S. Al Hallaj, J. Prakash, J.R. Selman, Characterization of commercial Li-ion batteries

using electrochemical – calorimetric measurements, J. Power Sources. (2000) 186–

194.

[28]    S. Al Hallaj, R. Venkatachalapathy, J. Prakash, J.R. Selman, Entropy Changes Due to

Structural Transformation in the Graphite Anode and Phase Change of the LiCoO2

Cathode, J. Electrochem. Soc. 147 (2000) 2432–2436. doi:10.1149/1.1393549.

[29]    H.J. Bang, H. Yang, Y. Sun, J. Prakash, The Dependence of Heat Generation of

LixMn204 and LiAl 0o7Mn 1930 a397S0.03 on 300 Entropy Change (Compared by the

Isothermal Micro-Calorimetry Method), in: E.B. Yeager, J. Prakash (Eds.), Fundam.

Underst. Electrode Process. Mem. Profr. Ernest B. Yeager  Proc. Int. Symp.,

Pennington, NJ : Electrochemical Society, 2005: pp. 300–309.

[30]  M. Dubarry, V. Svoboda, R. Hwu, B. Yann Liaw, Incremental Capacity Analysis and Close-to-Equilibrium OCV Measurements to Quantify Capacity Fade in Commercial Rechargeable Lithium Batteries, Electrochem. Solid-State Lett. 9 (2006) A454–A457. doi:10.1149/1.2221767.

[31]  J.-S. Kim, J. Prakash, J.R. Selman, Thermal Characteristics of Li[sub x]Mn[sub 2]O[sub 4] Spinel, Electrochem. Solid-State Lett. 4 (2001) A141. doi:10.1149/1.1387224.

[32]  E.M. Perassi, E.P.M. Leiva, A theoretical model to determine intercalation entropy and enthalpy: Application to lithium/graphite, Electrochem. Commun. 65 (2016) 48–52. doi:10.1016/j.elecom.2016.02.003.

[33]  E.P.M. Leiva, E. Perassi, D. Barraco, Shedding Light on the Entropy Change Found for the Transition Stage II→Stage I of Li-Ion Storage in Graphite, J. Electrochem. Soc. 164 (2017) A6154–A6157. doi:10.1149/2.0231701jes.

[34]  C.P. Grey, N. Dupré, NMR studies of cathode materials for lithium-ion rechargeable batteries, Chem. Rev. 104 (2004) 4493–4512. doi:10.1021/cr020734p.

[35]  Y.J. Lee, C.P. Grey, 6Li Magic Angle Spinning Nuclear Magnetic Resonance Study of the Cathode Materials Li1+αMn2−αO4−δ The Effect of Local Structure on the Electrochemical Properties, J. Electrochem. Soc. 149 (2002) A103. doi:10.1149/1.1429225.

[36]  B. Wu, V. Yufit, Y. Merla, R.F. Martinez-Botas, N.P. Brandon, G.J. Offer, Differential thermal voltammetry for tracking of degradation in lithium-ion batteries, J. Power Sources. 273 (2015) 495–501. doi:10.1016/j.jpowsour.2014.09.127.

[37]    G. Ceder, A. Van Der Ven, Phase diagrams of lithium transition metal oxides :

investigations from first principles, Electrochim. Acta. 45 (1999) 131–150.

doi:http://dx.doi.org/10.1016/S0013-4686(99)00199-1.

[38]    H. Abiko, M. Hibino, T. Kudo, Temperature Dependence of the Potential-Composition

Profiles of Li x Mn2 O 4 Spinel, Electrochem. Solid-State Lett. 1 (1998) 114–116.

doi:10.1149/1.1390655.

[39]    T. Ohzuku, M. Kitagawa, T. Hitai, Electrochemistry of Manganese Dioxide in Lithium

Nonaqueous Cell II. X-Ray Diffractional and Electrochemical Characterization on Deep

Discharge Products of Electrolytic Manganese Dioxide, J. Electrochem. Soc. 137

(1990) 40–46. doi:10.1149/1.2096421.

[40]    W. Liu, K. Kowal, C.G. Farrington, Mechanism of the Electrochemical Insertion of

Lithium into LiMn[sub 2]O[sub 4] Spinels, J. Electrochem. Soc. 145 (1998) 459.

doi:10.1149/1.1838285.

[41]    Y.J. Lee, F. Wang, S. Mukerjee, J. McBreen, C.P. Grey, 6Li and 7Li magic-angle spinning

nuclear magnetic resonance and in situ x-ray diffraction studies of the charging and

discharging of LixMn2O4 at 4 V, J. Electrochem. Soc. 147 (2000) 803–812.

doi:10.1149/1.1393276.

[42]    Y. Gao, J.N. Reimers, J.R. Dahn, Changes in the voltage pro le of Li/Li 1-xMn2-xO4 cells

as a function of x, Phys. Rev. B. 54 (1996) 3878–3883. doi:10.1103/PhysRevB.54.3878.

[43]    R.J. Gummow, An Investigation of Spinel-Related and Orthorhombic LiMnO[sub 2]

Cathodes for Rechargeable Lithium Batteries, J. Electrochem. Soc. 141 (1994) 1178.

doi:10.1149/1.2054893.

[44]   A. Van Der Ven, C. Marianetti, D. Morgan, G. Ceder, Phase transformations and volume changes in spinel LixMn2O4, Solid State Ionics. 135 (2000) 21–32. doi:10.1016/S0167-2738(00)00326-X.

[45]   A. Breitruck, H.E. Hoster, R.J. Behm, Short-range order in a metal - Organic network, J. Phys. Chem. C. 113 (2009) 21265–21268. doi:10.1021/jp908748w.

[46]   H.E. Hoster, Surface Alloys, in: Surf. Interface Sci. Prop. Compos. Surfaces Alloy. Compd. Semicond., 2014: pp. 329–367.

[47]   A. Bergbreiter, H.E. Hoster, S. Sakong, A. Groß, R.J. Behm, Energetics driving the short-range order in CuxPd1–x/Ru(0001) monolayer surface alloys, Phys. Chem. Chem. Phys. 9 (2007) 5127. doi:10.1039/b705237p.

[48]   T. Waldmann, D. Ku, H.E. Hoster, A. Groß, R.J. Behm, Oxidation of an Organic Adlayer : A Bird ' s Eye View, J. Am. Chem. Soc. 134 (2012) 8817–8822.

[49]   M. P. Mercer, H. E. Hoster, Ultrahigh vacuum and electrocatalysis - The powers of quantitative surface imaging, Nano Energy. 29 (2016) 394–413. doi:10.1016/j.nanoen.2016.04.015.

[50]   A. Bergbreiter, O.B. Alves, H.E. Hoster, Entropy effects in atom distribution and electrochemical properties of AuxPt1-x/Pt(111) surface alloys, ChemPhysChem. 11 (2010) 1505–1512. doi:10.1002/cphc.201000105.

[51]   J.-W. Song, C. Cuong Nguyen, H. Choi, K.-H. Lee, K.-H. Han, Y.-J. Kim, S. Choy, S.-W. Song, Impacts of Surface Mn Valence on Cycling Performance and Surface Chemistry of Li- and Al-Substituted Spinel Battery Cathodes [J. Electrochem. Soc., 158, A458 (2011)], J. Electrochem. Soc. 158 (2011) A458–A464. doi:10.1149/1.3578404.

[52]   L. Guohua, The Spinel Phases LiMyMn 2−yO4 (M = Co, Cr, Ni) as the Cathode for

Rechargeable Lithium Batteries, J. Electrochem. Soc. 143 (1996) 178.

doi:10.1149/1.1836405.

[53]   A. Van Der Ven, C. Marianetti, D. Morgan, G. Ceder, Phase transformations and

volume changes in spinel Li x Mn 2 O 4, Solid State Ionics. 135 (2000) 21–32.

[54]   J. Sugiyama, T. Atsumi, A. Koiwai, T. Sasaki, T. Hioki, S. Noda, N. Kamegashira, The

effect of oxygen deficiency on the structural phase transition and electronic and

magnetic properties of the spinel LiMn2O4−δ, J. Phys Condens. Matter. 9 (1997)

1729–1741.

[55]   K. Momma and F. Izumi, VESTA 3 for three-dimensional visualization of crystal,

volumetric and morphology data., J. Appl. Crystallogr. 44 (2011) 1272–1276.

[56]   G.S. Karlberg, T.F. Jaramillo, E. Skúlason, J. Rossmeisl, T. Bligaard, J.K. Nørskov, Cyclic

voltammograms for H on Pt(111) and Pt(100) from first principles, Phys. Rev. Lett. 99

(2007) 1–4. doi:10.1103/PhysRevLett.99.126101.

[57]   N. Metropolis, A.W. Rosenbluth, M.N. Rosenbluth, A.H. Teller, E. Teller, Equation of

State Calculations by Fast Computing Machines, J. Chem. Phys. 21 (1953) 1087–1092.

doi:doi:10.1063/1.1699114.

[58]   K. Binder, D. Landau, Phase diagrams and critical behavior in Ising square lattices with

nearest- and next-nearest-neighbor interactions, Phys. Rev. B. 21 (1980) 1941–1962.

doi:10.1103/PhysRevB.21.1941.

[59]   L.D. Landau, E.M. Lifshitz, Statistical Physics, Third Edit, Pergamon, Oxford, 1975.

[60]   G.H. Meier, Thermodynamics of Surfaces and Interfaces: Concepts in Inorganic

Materials., Cambridge Univ Press, 2014.

[61]    T. Kudo, M. Hibino, Theoretical dependences of the free energy and chemical

potential upon composition in intercalation systems with repulsive interaction

between guest ions, Electrochim. Acta. 43 (1998) 781–789. doi:10.1016/S0013-

4686(97)00205-3.

[62]    G.L. Plett, Recursive approximate weighted total least squares estimation of battery

cell total capacity, J. Power Sources. 196 (2011) 2319–2331.

doi:10.1016/j.jpowsour.2010.09.048.

[63]    J.M. Cowley, Short-range order and long-range order parameters, Phys. Rev. 138

(1965) A1384. doi:10.1103/PhysRev.138.A1384.



<InlineImage1>
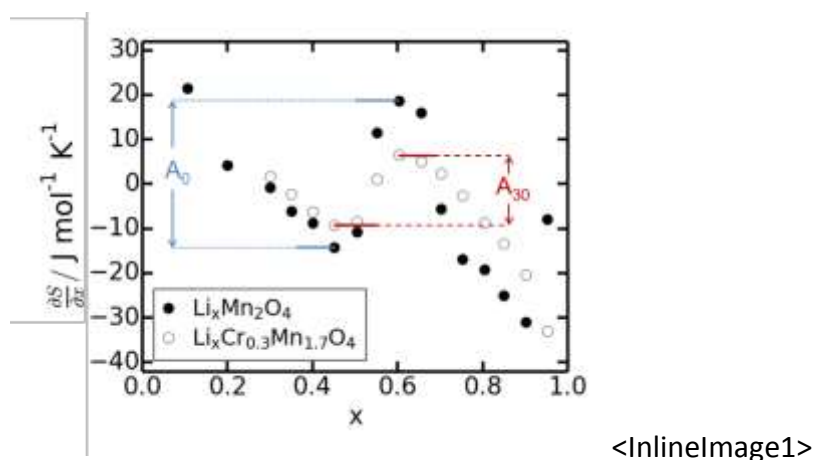
Figure 1. Example of an entropy profile, shown for two different electrode compositions as indicated in the legend. Replotted based on the data presented elsewhere in Figure 1 of ref. [21]. The significance of the combined entropy peak amplitudes, $A_0$ and $A_{30}$, referring to 0 and 30 % defect substitution respectively, is described in the main text.
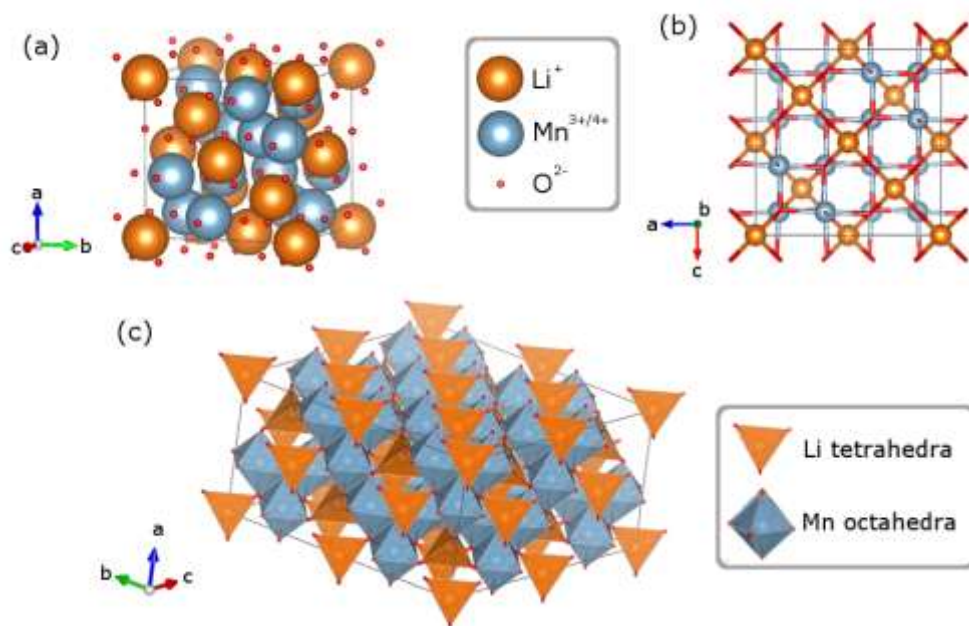
Figure 2. (a) Spinel structure of $Li_xMn_2O_4$, (b) top down view of the unit cell, (c) (2 x 2 x 1) supercell, showing the tetragonal bonding of Li to oxygen and the octahedral bonding of O to Mn. The figure was produced using VESTA 3 [55].
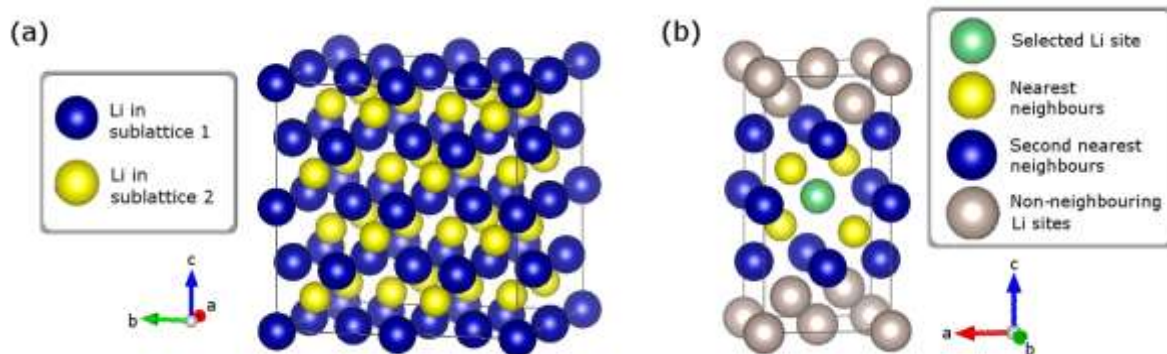


Figure 3. (a) Representation of (2x2x1) supercell of the diamond lattice in which Li resides. The two sublattices are indicated in blue and yellow respectively. Each sublattice has fcc symmetry. (b) (2x1x1) diamond supercell. The nearest and second nearest neighbours in the model are represented. These are the sites that are addressed within the pairwise interaction model. It has 4 nearest neighbours in the yellow sublattice, and 12 second nearest neighbours in the blue sublattice. The figure was produced using VESTA 3 [55].
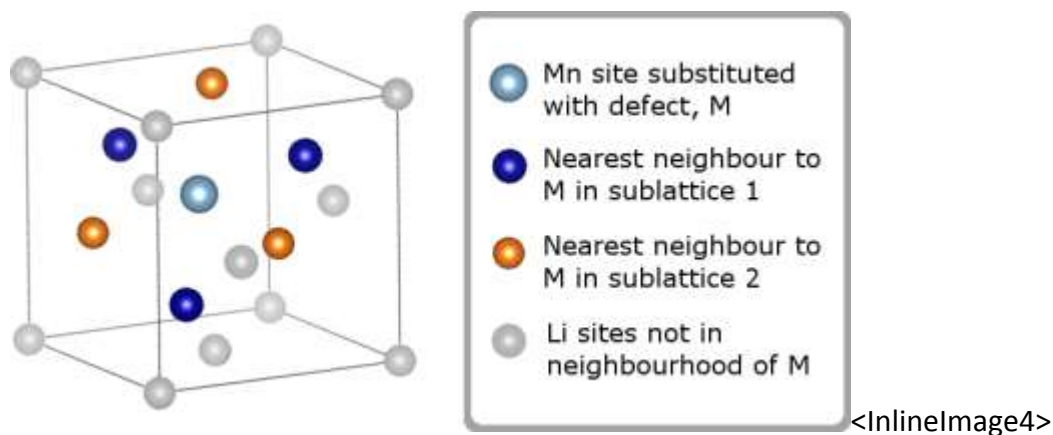
Figure 4. Representation of the Li diamond lattice. One of the sites from the spinel lattice, representing a substitutional defect, is shown in light blue. The nearest Li neighbour sites to this defect are highlighted in gold and dark blue, dependent upon the sublattice in which the Li atom is found. It can be seen that the nearest Li neighbour sites to the defect, which are the sites in which one pinned Li atom per defect M is presumed to reside, would be distributed equally amongst the two sublattices. The figure was produced using VESTA 3 [55].
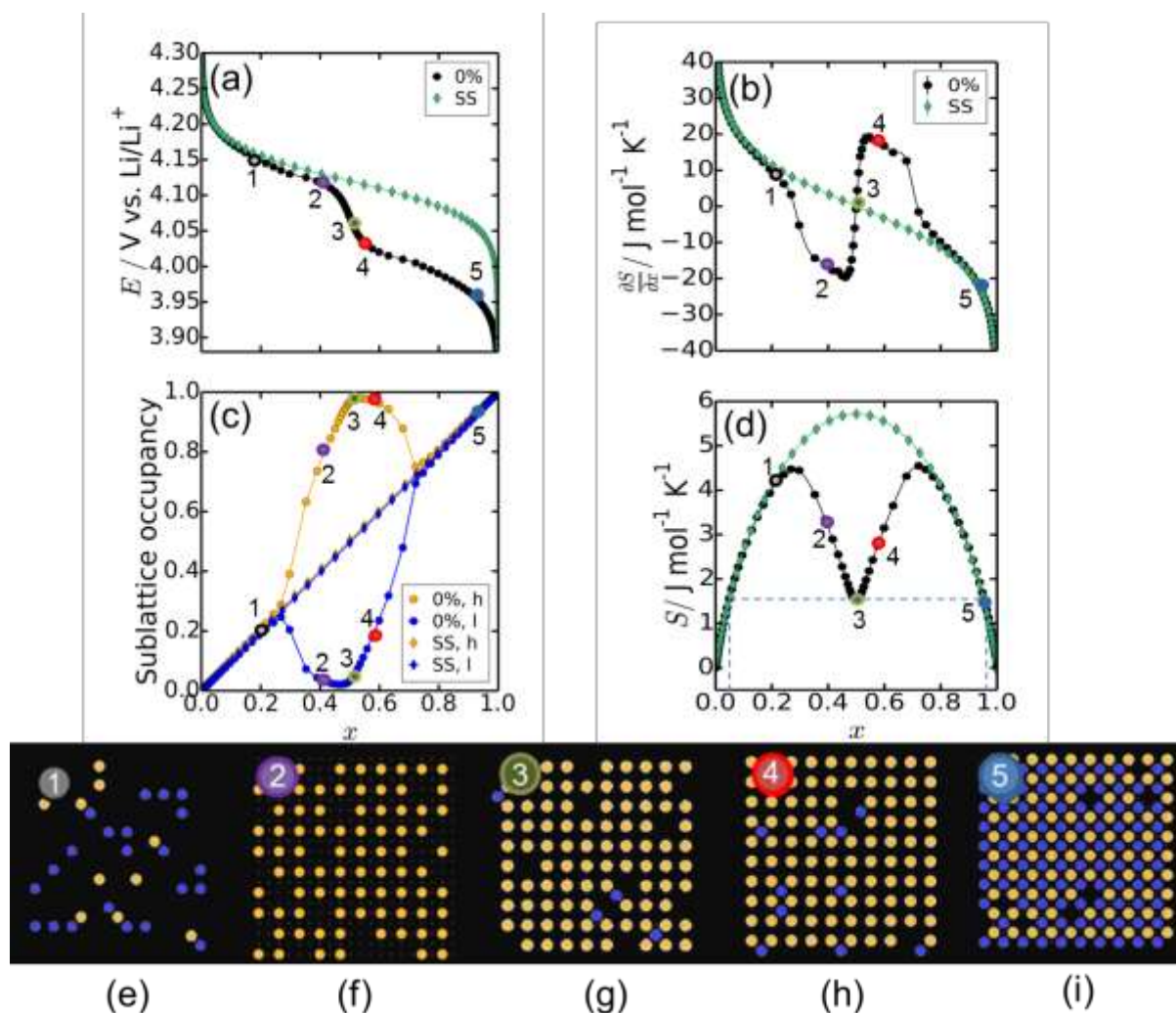
Figure 5. Variation of (a) electrode potential, (b) partial molar entropy change, (c) occupancy in each of the sublattices (here, the sublattice with the highest occupation is indicated in gold) and (d) configurational entropy, plotted as a function of the amount of intercalated Li, $x$, for $Li_xMn_2O_4$ ($y$ = 0 %) and a solid solution (SS) with $\varepsilon$ = 4.12 eV and no lateral Li-Li interactions. In (c), "h" and "l" refer to the highest and lowest occupied sublattices, respectively. The significance of the blue dashed lines in (d) is described in the main text. (e-g) Snapshots of the lattice at selected electrode potential values (e) $E$ = 4.150 V, (f) $E$ = 4.115 V, (g) $E$ = 4.050 V, (h) $E$ = 4.025 V, (i) $E$ = 3.950 V. The pictures were produced by projecting a layer of 1 unit cell thickness from the overall 10 x 10 x 10 lattice onto a 2D plane for $Li_xMn_2O_4$ ($y$ = 0 %). The relevant points on each of the plots (a-d) relating to the pictures are labelled 1-5 for ease of comparison.
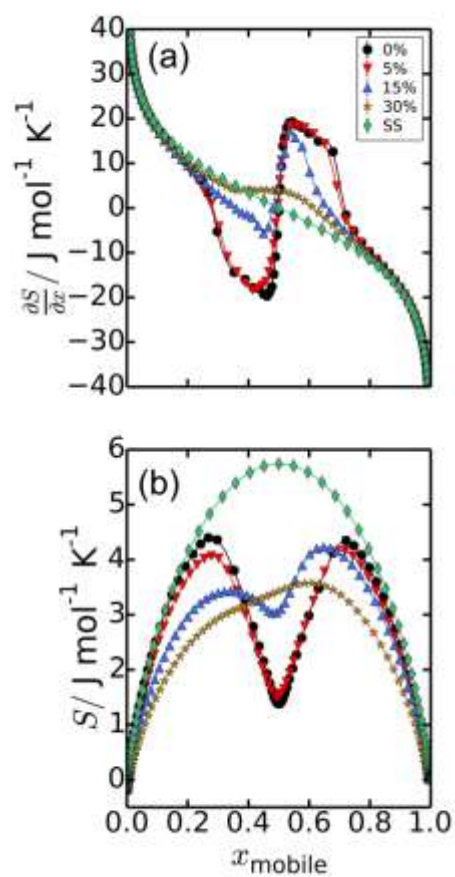
Figure 7. (a) The partial molar entropy, $\partial S/\partial x$, and (b) the configurational entropy, $S$. The defect percentage is indicated in the legend. The results are overlaid with the ones expected for a solid solution, SS.
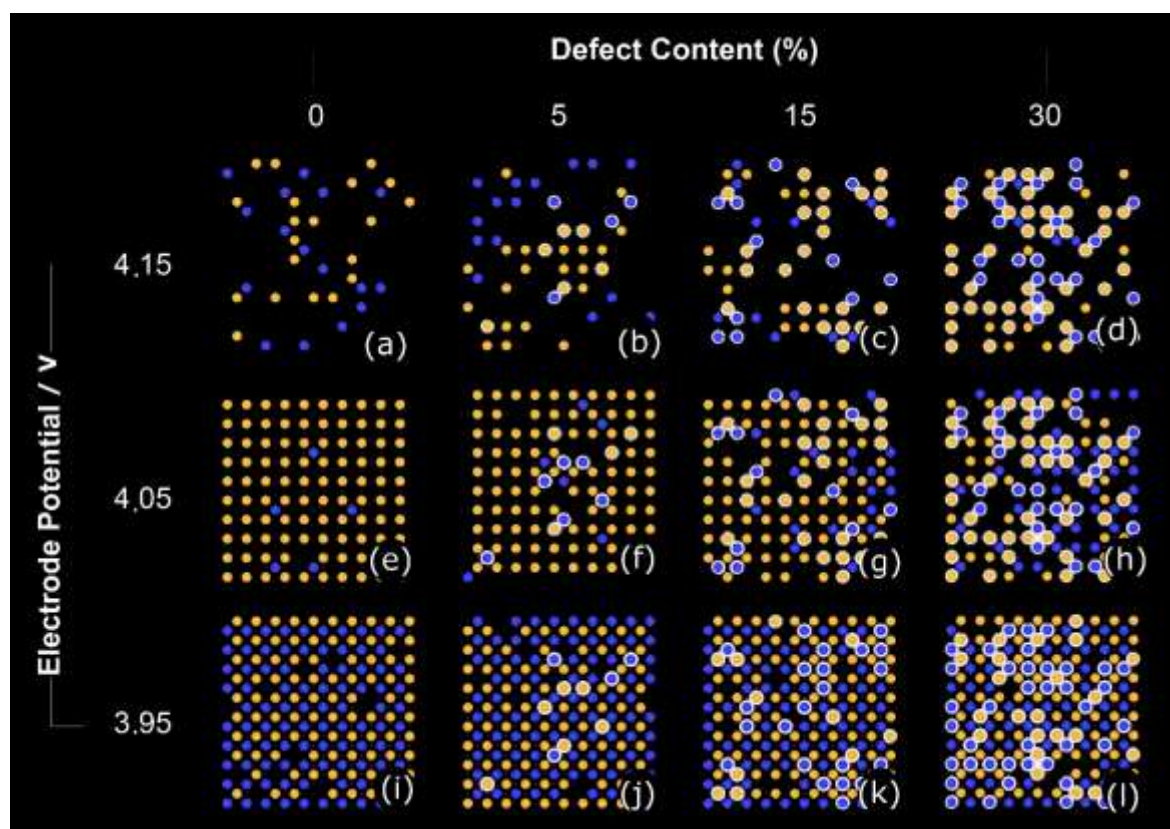
Figure 8. Comparison of the equilibrium lattice state for y = 0% (left column, a,e,i), y = 5% (second column, b,f,g), y = 15% (third column, c,g,k) and y = 30 % (right column, d,h,k). The Li sites that are pinned are indicated with white circles.
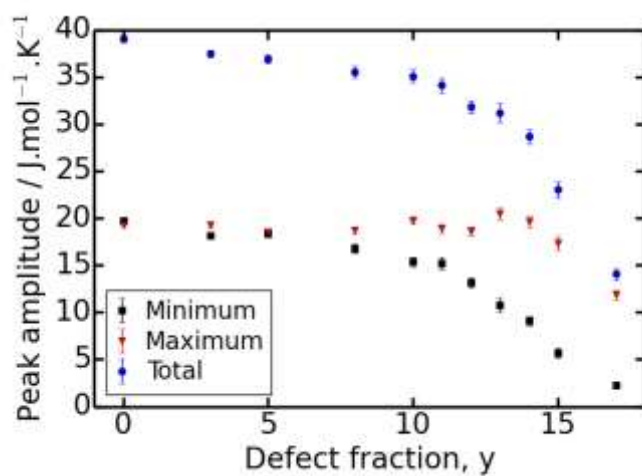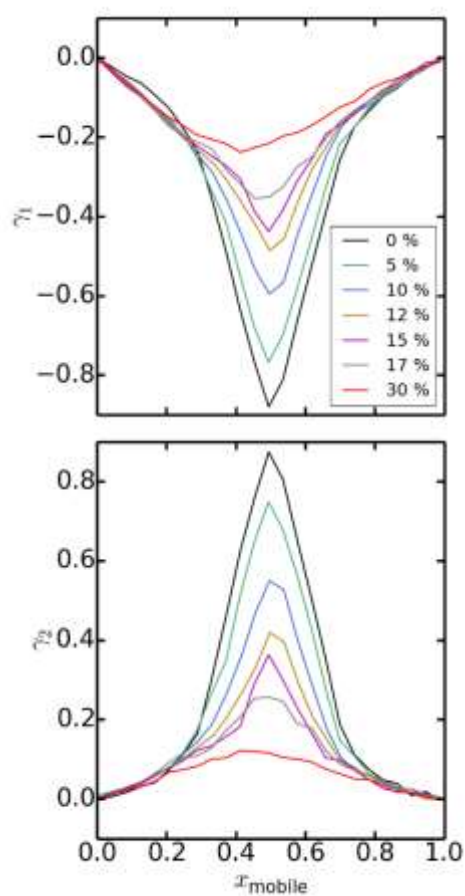
Figure 9. Variation in the absolute amplitudes of the peaks as a function of the defect content. The overall amplitude in the partial molar entropy, defined in Figure 1, is shown along with the amplitudes of the two individual peaks.
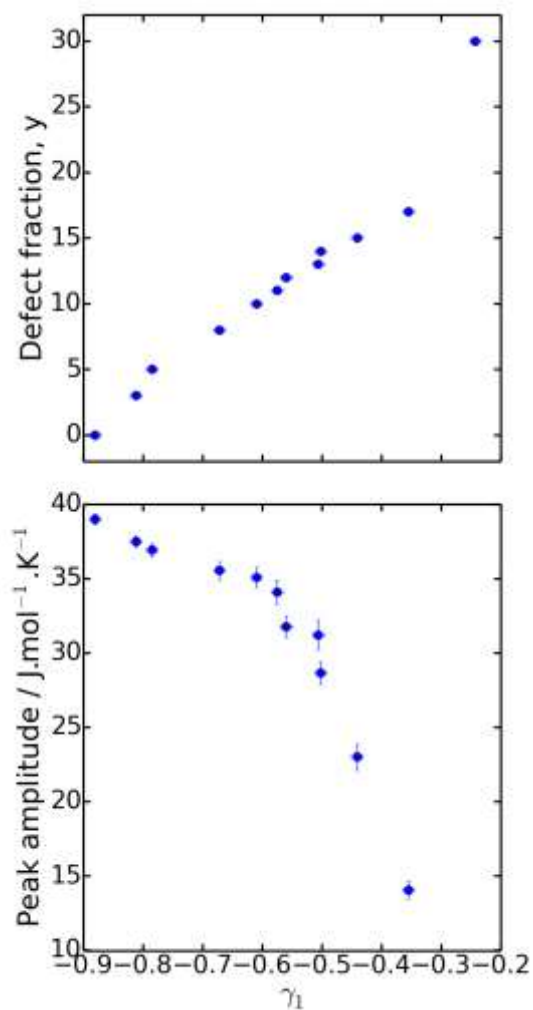
(a)

<InlineShape4>



<InlineImage10>

Figure 10. Variation in the short range order parameter due to (a) nearest neighbours and (b) second nearest neighbours. The defect fraction is shown in the legend.

(a)

<InlineShape2>

<InlineImage11>

Figure 11. Plot of (a) the defect fraction, *y*, and (b) the entropy peak amplitude as a function of the first

Warren-Cowley parameter, $\gamma_1$.

Table 1. Comparison of the results for the partial molar entropy peak amplitudes obtained from the simulations with experimental results. Because the experimental data were obtained from digitised graphs, they are reported to 2 significant figures. Within the Li pinning model, the simulated results are applicable to both defects.

| Defect concentration | Experimental $\partial S/\partial x$ peak amplitude / J mol$^{-1}$ K$^{-1}$ | Simulated $\partial S/\partial x$ peak amplitude / J mol$^{-1}$ K$^{-1}$ | Experimental Defect |
|---|---|---|---|
| 0 % | 41 [13], 33 [14],34 [21] | 39.0 ± 0.4 | N/A |

| 5 % | 33 [25] | 36.9 ± 0.5 | Cr |
| | 27 [25] | | Co |
| 15 % | 23 [25] | 23.0 ± 0.9 | Cr |
| | 23 [25] | | Co |
| 30 % | 17 [25], 16 [21] | Not resolved | Cr |
| | 16 [25] | | Co |